Supporting Information for

# Steric Effects Control Dry Friction of H- and F-Terminated Carbon Surfaces

Thomas Reichenbach[a,b], Leonhard Mayrhofer[a,d], Takuya Kuwahara[a], Michael Moseler[a-d], and Gianpietro Moras[a,*]

[a] *Fraunhofer IWM, MicroTribology Center μTC, Wöhlerstraße 11, 79108 Freiburg, Germany*
[b] *Institute of Physics, University of Freiburg, Hermann-Herder-Straße 3, 79104 Freiburg, Germany*
[c] *Freiburg Materials Research Center, University of Freiburg, Stefan-Meier-Straße 21, 79104 Freiburg, Germany*
[d] *Cluster of Excellence livMatS @ FIT – Freiburg Center for Interactive Materials and Bioinspired Technologies, University of Freiburg, Georges-Köhler-Allee 105, 79110 Freiburg, Germany*
[*] *E-mail: gianpietro.moras@iwm.fraunhofer.de*

# 1 Chemical Stability of H/F-Terminated Carbon Surfaces

In order to verify the chemical stability of H/F-terminated diamond and DLC surfaces and further justify the use of a non-reactive force field, we performed an additional series of large-scale self-consistent-charge density-functional tight-binding (DFTB) MD simulations[1] as implemented in the Atomistica code.[2]

Using this approach we have recently investigated tribochemical processes taking place at similar interfaces (see e.g. Kuwahara et al.[3]). The simulations described in this publication show that, during running-in, unterminated diamond surfaces in contact with water become chemically terminated by H atoms and OH groups produced by dissociative chemisorption of the water molecules. After this running-in phase, once the surfaces are fully terminated, no chemical reaction is observed during ns-long sliding simulations even at normal loads as high as 10 GPa. This results in a stable low-friction regime which is also visible in experimental investigations (see, for instance, Konicek et al.[4], where superlow friction is stable for thousands of friction cycles).

The present manuscript addresses exactly this steady-state low-friction regime, where no chemical transformation of the chemical termination occur for a long time after running-in. To confirm that this also holds in the presence of F terminations, we explicitly ran 1-ns-long DFTB simulations with a sliding speed of 100 m/s under 5 GPa normal load for the fully commensurate 50H/50-B and 75H/25F cases (Fig. 2, main text), i.e. the cases with the largest corrugation and frictional stress. The systems consist of a $2 \times 2$ repetition of the unit cells shown in Fig. 1a of the main text and each slab has 12 layers with 16 C atoms, the surfaces far from the interface are hydrogen terminated. Three-dimensional periodic boundary conditions are imposed with a cell size of $8.73 \times 10.07 \times 50$ Å$^3$. The outermost two C layers and their terminations are kept rigid and the normal pressure $P_N$ is applied using Pastewka's pressure coupling algorithm with a damping force.[5] After equilibration of the systems at the externally imposed load, a constant velocity of 100 m/s is imposed to the upper rigid layer while keeping the normal load applied. The equations of motion are integrated with time step $\Delta t = 0.5$ fs, a Langevin thermostat is used to thermalize the atoms far from the interface at a $T = 300$ K. In the calculation of the temperature for the thermostat, the center-of-mass motion of the respective atoms is subtracted. In line with the fact that the C-F bond is even stronger than the C-H and C-O bonds,[6] we do not observe any chemical reaction and the full bond network remains unchanged upon sliding. Snapshots of both simulations before and after sliding are shown in Fig. S1a and S1b.

To check if H/F-terminated ta-C surfaces are also chemically stable, we prepared two ta-C samples using the same protocol and density as for the large-scale non-reactive ta-C simulations (see section 12) and performed 1-ns-long DFTB simulations with a 50H/50F ratio, where the largest shear stress is expected. Snapshots of the system before and after sliding are shown in Fig. S1c. Also in these cases, we observe no chemical reaction involving the sliding interfaces that remain chemically stable throughout the simulation. A very limited amount of occasional chemical events (3 bond breaking and 6 bonds formations in total) are observed within the ta-C slabs. These events are C-C bond formation and/or breaking that can be traced back to the preparation of the amorphous networks, that are inevitably

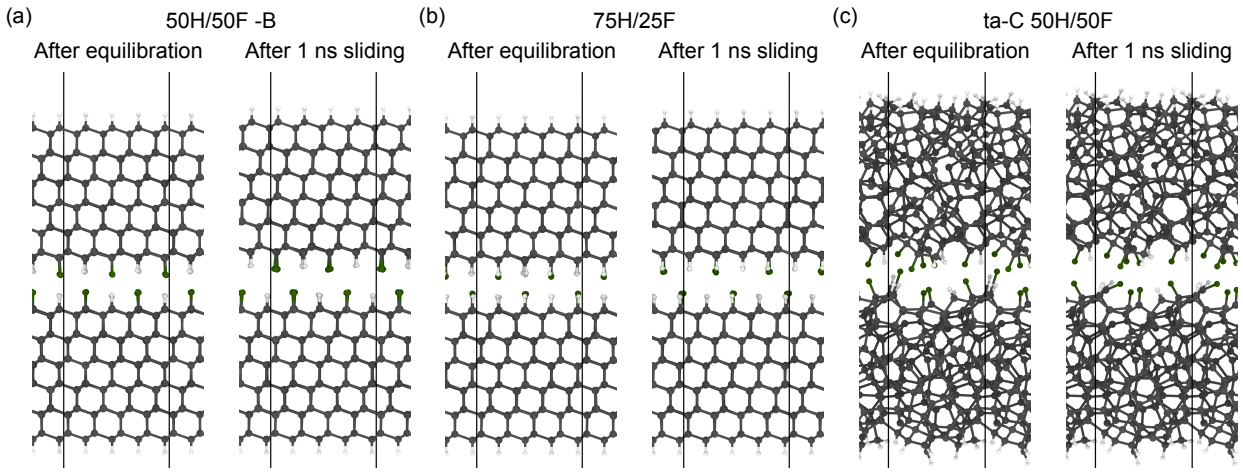


Figure S1: Snapshots of the (a) 50H/50F-B, (b) the 75H/25F and (c) the 50H/50F ta-C systems after pressure and temperature equilibration (left), and after sliding for 1 ns (right).

metastable. If our method of preparing the ta-C samples included additional DFTB uniform shear of the bulk samples for several nanoseconds (to mimic a running-in phase), a "less meta-stable" amorphous structure would form and no more chemical reactions would occur.

# 2 Force-Field Parameters for H/F-Terminated C(111) Systems

The explicit functional form of the all-atom classical force field (FF) for H/F-terminated C(111) surfaces is given in the main text. It consists of bonded interactions (harmonic bonds and angles) and nonbonded interactions (a Coulombic and a Lennard-Jones (LJ) term). The following conventions are used:

- Bulk diamond is only described by harmonic bonds and angles. There is no nonbonded interaction between bulk C atoms (i.e. C atoms that are not terminated by H or F). Note that there is nonetheless a LJ interaction between bulk C atoms and H/F-terminated C atoms according to the combination rules given in the main text. This convention leads to two significant advantages: (i) the bond and angle parameters that determine diamond's elastic constants can be adjusted mostly independent of the nonbonded parameters; (ii) we can exclude nonbonded interactions between bulk diamond atoms in the neighbor lists. As the vast majority of the atoms in the large-scale sliding simulations are bulk C atoms (about 98.9%), this results in a speed-up of more than a factor two.

- Following the conventions used in the OPLS force field,[7] nonbonded interactions are used between atoms that are separated by at least 4 bonds. For atoms separated by 3 bonds the nonbonded interaction is halved.

- For simplicity, all C atoms (C in bulk diamond, C bonded to H, C bonded to F) have the same LJ parameters. Moreover, all bonds and angles involving C atoms only have identical bonds and angles parameters.

With these conventions we use the following scheme to find a suitable parameter set. Standard OPLS values for hydrocarbons and perfluorocarbons serve as initial guesses.[7,9]

1. Bonds lengths of C-C, C-F and C-H bonds are taken from optimized DFT structures. The distance $r_{eq,\mathrm{CC}}$ between C atoms is chosen to be 1.539 Å, corresponding to the diamond lattice constant of 3.554 Å, as optimized with PBE-TS09. $r_{eq,\mathrm{CF}} = 1.371$ Å and $r_{eq,\mathrm{CH}} = 1.11$ Å are taken from the optimized C(111) surface structures with pure H/F terminations. The equilibrium angle $\theta_{eq}$ for all three-body terms is chosen to be 109.5° corresponding to diamond's cubic structure.

2. $k_{r,\mathrm{CC}}$ and $k_{\theta,\mathrm{CCC}}$ are adjusted in order to closely reproduce the experimental values of the elastic constants.[8] This yields $k_{r,\mathrm{CC}} = 15.21$ eV/Å$^2$ and $k_{\theta,\mathrm{CCC}} = 4.304$ eV/rad$^2$. A comparison between the obtained and experimental elastic constants can be found table S1.

3. In order to make a reliable statement about electrostatic interactions, we need to ensure that Coulombic and non-Coulombic interactions are separated correctly, i.e. the electric field generated by the point charge parameters in the force field should reproduce the DFT electric field. Therefore, the electrostatic potential atomic charges $q_{\mathrm{F}} = -0.2|e|$ and $q_{\mathrm{H}} = 0.09|e|$ obtained from DFT and published in an earlier study are used.[10] The C atoms bonded to H or F carry the corresponding countercharge. Bulk C have zero charge.

4. The contact potential energy surface (CPES) plays a crucial role in friction.[11–13] Therefore, the $\varepsilon$ and $\sigma$ LJ-Parameters of C, H and F atoms are adjusted in order to correctly reproduce the CPES as described in the main text. A good agreement between the FF and DFT CPES is obtained with the following parameters: $\sigma_{\mathrm{F}} = 3.1$ Å, $\sigma_{\mathrm{H}} = 2.05$ Å, $\sigma_{\mathrm{C}} = 4.0$ Å, $\varepsilon_{\mathrm{F}} = 0.00122$ eV, $\varepsilon_{\mathrm{H}} = 0.00138$ eV, $\varepsilon_{\mathrm{C}} = 0.00206$ eV.

5. $k_{r,\mathrm{CH}}$ and $k_{r,\mathrm{CF}}$ are adjusted to reproduce DFT distance-energy curves upon elongation and compression of individual C-H and C-F bonds on purely terminated C(111) surfaces, yielding $k_{r,\mathrm{CH}} = 14.744$ eV/Å$^2$ and $k_{r,\mathrm{CF}} = 15.914$ eV/Å$^2$.

Table S1: Comparison of bulk elastic constants of diamond determined experimentally and by using the force field presented here.

| | Experiment[8] | Force Field |
|---|---|---|
| $C_{11}$ (GPa) | 1080 | 1112 |
| $C_{12}$ (GPa) | 127 | 130 |
| $C_{44}$ (GPa) | 577 | 503 |
| Young's modulus (GPa) | 1054 | 1085.0 |
| Poisson's ratio | 0.105 | 0.104 |

6. $k_{\theta,\mathrm{CCH}}$ and $k_{\theta,\mathrm{CCF}}$ are obtained by bending individual H/F atoms on purely terminated C(111) surfaces in different directions while keeping the bond length fixed. $k_{\theta,\mathrm{CCF}} = 2.168$ eV/rad$^2$ and $k_{\theta,\mathrm{CCH}} = 1.826$ eV/rad$^2$ result in a good agreement of the DFT and FF angle-energy curves.

# 3 Energy-Distance Curves of H/F-Terminated C(111) Surfaces

In order to assess the accuracy of the parameter set described in section 2 for systems under normal load, we measure how the potential energy of the 100H/0F, 75H/25F, 50H/50F-A, 25H/75F and 0H/100F self-mated systems varies as a function of the distance between the two surfaces. We do this for one relative position of the upper and lower slab. For each considered value of the distance between the two slabs, the atomic structure is relaxed while the outermost bottom and top carbon layers and their terminations are kept rigid. The energy-distance curves calculated with DFT and with the FF are plotted in Fig. S2 and a good agreement between the two methods can be observed.

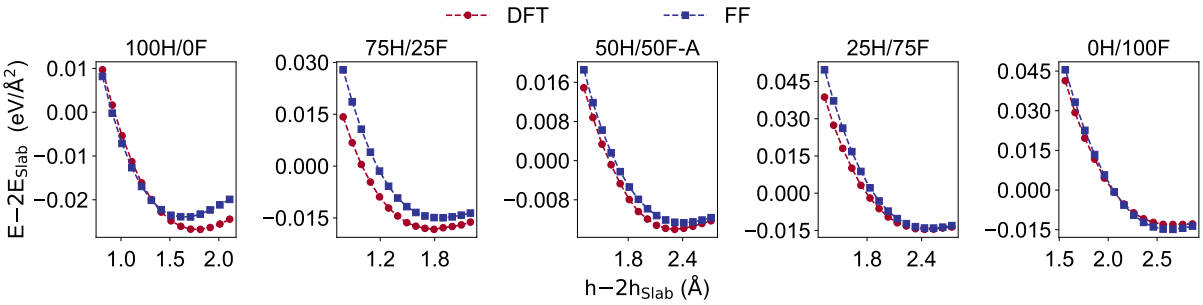


Figure S2: Energy-distance curves for self-mated H/F-terminated C(111) surfaces. $h_{\mathrm{Slab}}$ and $E_{\mathrm{Slab}}$ correspond to the height and potential energy of an isolated slab, $h$ and $E$ denote the height and energy of the total system.

# 4 Role of the Electronic Charge Redistribution in the CPES

A recent work by Wolloch et al.[14] revealed a close relation between the interfacial charge redistribution due to inter-slab interactions and the CPES corrugation. As such redistribution is not captured by a non-reactive force field, we need to ensure that the influence of the charge redistribution is negligible for CPES corrugation of the investigated systems.

For this purpose, using the example of Fig. 1e in the main text, we follow two steps:

1. First, we separate the DFT CPES into the contribution of the TS09 van-der-Waals correction and the uncorrected PBE energies. As apparent from Fig. S3a, the largest contribution to the corrugation stems from the TS09 energy variations.

2. Secondly, we investigate how strongly the TS09 correction is affected by the electronic charge redistribution due to inter-slab interactions. Within the TS09 approach, the Hirshfeld partitioning of the electron density is used to determine the effective volume of the atoms.[15] There is no further dependence on the electron density. The role of the charge redistribution can thus be assessed by replacing the actual electron density used in the Hirshfeld partition with the sum of the electron densities of the individual, isolated slabs. A comparison between the PBE-TS09 CPES corrugation and the PBE-TS09 CPES corrugation, where this "non-redistributed" electron density was used for the TS09 correction, is shown in Fig. S3b. The electronic charge redistribution does not influence the CPES significantly. Combined with our previous work[10] that shows that the electric field of the considered surfaces can be modeled using a point charge model, this justifies our way of treating inter-slab interaction by using a non-reactive force field.

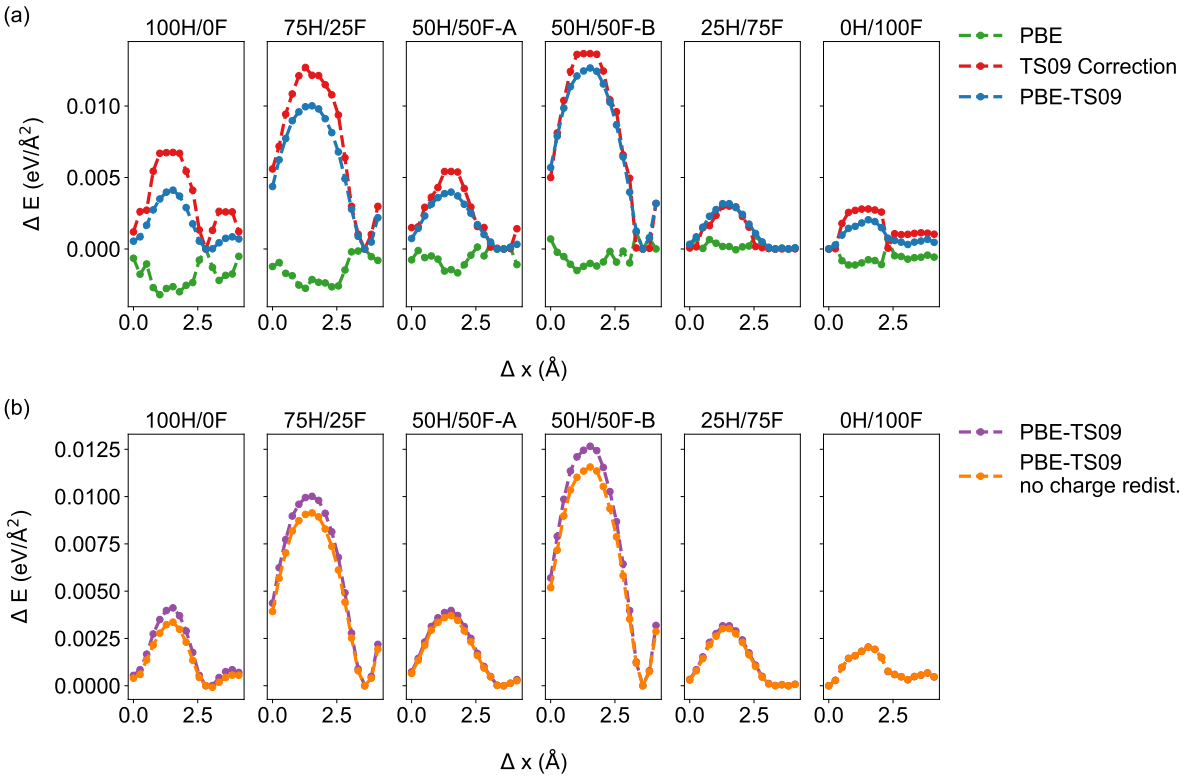


Figure S3: (a) TS09 (red) and PBE (green) contributions to the PBE-TS09 CPES (blue) of Fig. 1e in the main text. (b) Comparison between the PBE-TS09 CPES (violet) and the CPES, where the sum of the electron densities of the isolated, individual slabs was used in the TS09 correction (orange).

# 5 Correlation between CPES and Variation of the Inter-Slab Separation

In Fig. S4 the DFT energy profile depicted in Fig. 1e in the main text is shown alongside the variation of the inter-slab distance (note that the slabs are rigid). The fact that both curves closely follow each other suggests a strong correlation between geometric and energetic corrugation.

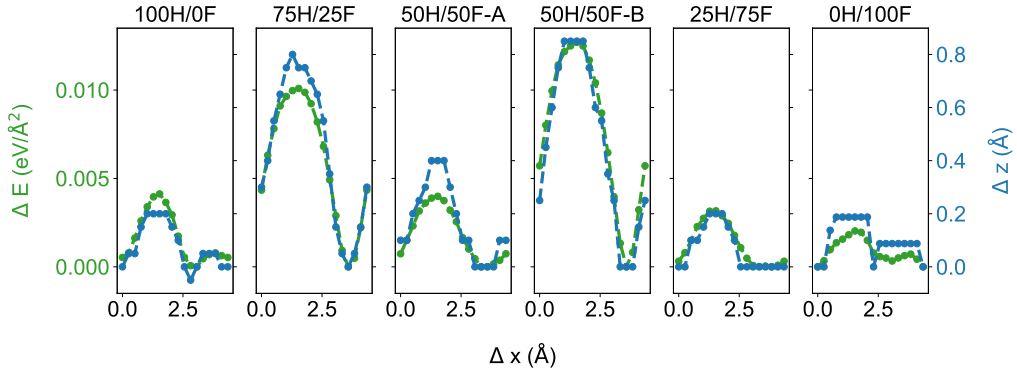


Figure S4: DFT energy variation (green) and inter-slab distance variation (blue) for self-mated H/F-terminated C(111) surfaces. The energies and distances are given with respect to the minimal energy along the path and its respective slab separation.

# 6 Determination of the Sliding Paths

The terminations of the upper and lower slab of fully commensurate systems undergo a collective motion in order to circumvent head-on collisions. As a result, the sliding path can be described by the evolution of the average relative displacement between the terminations of the upper and lower slab. For each configuration of the system along the sliding trajectory this average relative displacement is determined by:

1. Calculating the displacement of each termination in $x$ and $y$ direction with respect to the initial relaxed configuration of widely separated surfaces using the minimum image convention. This yields a $2N$-dimensional displacement vector per surface, where $N$ is the number of terminations per surface.

2. Subtracting the displacement vector of the lower slab from the displacement vector of the upper slab and taking the mean in $x$ and $y$.

The paths shown in Fig. 3 of the main text are calculated by folding back the average relative $x$ displacements of each image into the unit cells and averaging the absolute values of the $y$ mean displacements in bins of $\Delta x = 0.15$ Å.

# 7 System-Size Dependence of the Sliding Path and the Shear Stress

The lateral stiffness of the simulation slabs depends on their height, which usually influences friction.[16] As illustrated for the 75H/25F case in Fig. S5a, we find that the shear stress (squares) roughly converges to a constant value (within error bars) for increasing values of slab height. Closely related, also $\langle\tau\rangle_{\text{ideal}} = \sum_i \Delta E_i / l_x$ (Fig. S5a, triangles), obtained by NEB simulations, as well as the sliding path (Fig. S5b) show a similar convergence behavior. For the calculations described in the main text a height of 182 Å is used.

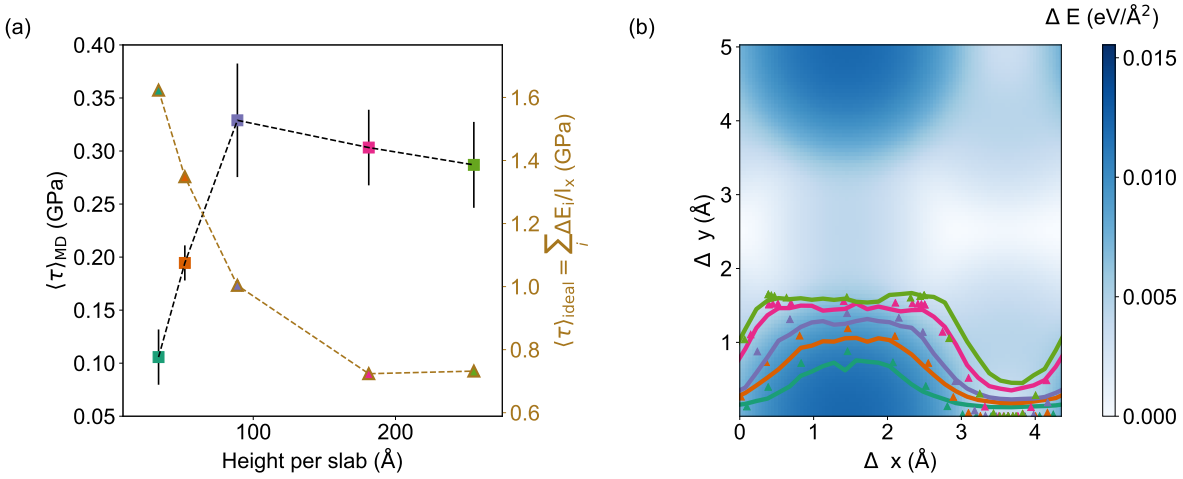


Figure S5: Dependence of the measured averaged shear stress $\langle\tau\rangle_{\text{MD}}$ (squares, a), the ideal shear stress $\langle\tau\rangle_{\text{ideal}} = \sum_i \Delta E_i / l_x$ (triangles, a) and the sliding path (b) on the system size for the 75H/25F C(111) sliding system. The height of the individual slabs is defined as the distance between the topmost and the lowest C atoms of an individual relaxed slab. The paths of the NEB calculations are marked as triangles in (b), solid lines refer to the measured paths during dynamic sliding simulations. The colors of lines and triangles refer the respective squares in (a), while the background is colored according to the 75H/25F CPES in Fig 1d of the main text.

Interestingly, although the height of the energy barriers for sliding decrease for increasing system height (i.e. decreasing stiffness), the shear stress increases before reaching the aforementioned plateau. This finding is in contrast with the observed correlation between $\langle\tau\rangle_{\text{ideal}}$ and the measured shear stress $\langle\tau\rangle_{\text{MD}}$ in Fig. 3c of the main text and highlights the crucial role of the stiffness of the tribosystem. This is due to the fact that friction decreases with decreasing CPES corrugation but increases with decreasing stiffness. Both these trends can be explained by the Prandtl-Tomlinson model as discussed in a recent review.[16] Throughout the main text an identical height of the system is chosen such that the frictional differences can be traced back to differences in the CPES.

# 8 Pressure Dependence of the Shear Stress

The pressure dependence of the shear stress for the 75H/25F system is shown in Fig. S6. Neglecting adhesion, Amontons' law states that the friction coefficient can be expressed by $\mu = \langle\tau\rangle \cdot \mathrm{P_N^{-1}}$. In this case, we obtain $\mu = 0.061$. If we consider adhesion, Amontons' law can be generalized to $\tau = \tau_0 + \mu \mathrm{P_N}$, where $\sigma_0$ is an adhesion-controlled shear stress. To calculate the friction coefficient in such case we take the slope of a linear fit (dashed line) and obtain $\mu = 0.067$. From this we conclude that the friction coefficient can be approximated using $\mu = \langle\tau\rangle \cdot \mathrm{P_N^{-1}}$ that only requires a single calculation rather than a set of calculations at different normal loads.

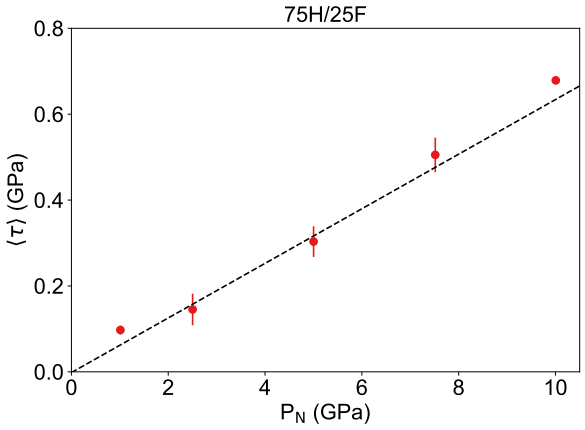


Figure S6: Shear stress $\langle\tau\rangle$ as a function of the applied normal pressure $\mathrm{P_N}$ for the 75H/25F case.

# 9 Effect of $\varepsilon$ on Friction

In general, an increased variation of the adhesive energy along the sliding path results in an increased CPES corrugation and hence in a larger shear stress. This variation is directly influenced by the $\varepsilon$ parameter.

However, for the investigated systems the energy corrugation (and in turn the shear stress) does not significantly change upon the $\varepsilon_\mathrm{H} \leftrightarrow \varepsilon_\mathrm{F}$ exchange as $\varepsilon_\mathrm{H}$ and $\varepsilon_\mathrm{F}$ are very similar. In addition, significant contributions to the LJ energy corrugation originate from the LJ interactions between the H/F terminations and C atoms of the opposite surface as well as from the LJ interaction between C atoms of opposing slabs. The former interaction is only slightly affected by the parameter exchange via the square-root dependence $\varepsilon_\mathrm{HC} = \sqrt{\varepsilon_\mathrm{H}\varepsilon_\mathrm{C}}$, while the latter interaction has no (direct) dependence. We explicitly show this in Fig. S7, which is a reproduction of the 0H/100F case of Fig. 1e of the main text, where additionally the corrugations upon different $\varepsilon$ variations are shown. Increasing $\varepsilon_\mathrm{F}$ by a factor 2 or 3, increases the sum of the barrier heights by a factor of 1.17 and 1.30, respectively. Doubling both $\varepsilon_\mathrm{F}$ and $\varepsilon_\mathrm{C}$ leads to an increase of a factor 1.74. In contrast, upon the $\varepsilon_\mathrm{F} \rightarrow \varepsilon_\mathrm{H}$ exchange,

the increase is only a factor 1.03 due, as mentioned above, to the similar values of the two parameters.

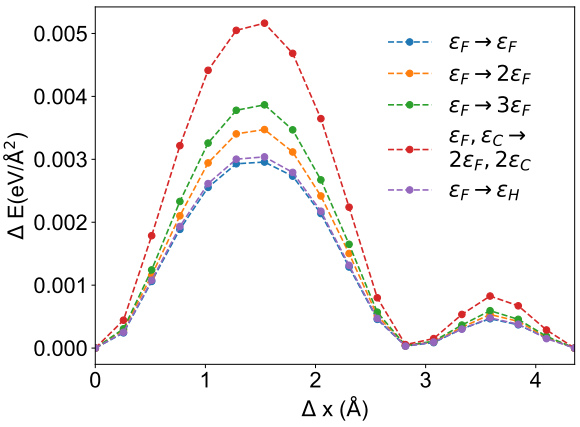


Figure S7: The CPES of the 0H/100F diamond system along the straight sliding path of Fig. 1e of the main text for different $\varepsilon$ exchanges.

This is true for rigid systems without an externally applied normal load (like in the case of Fig. 1e of the main text). However, our friction results are obtained for systems that are allowed to elastically deform and slide under an external load. In such case, the systems experience a strong LJ repulsion. To assess the influence of $\varepsilon$ under these conditions, we performed the 0H/100F MD sliding simulation of Fig. 3a with $\varepsilon_{\mathrm{F}} \rightarrow 2\varepsilon_{\mathrm{F}}$ and $\varepsilon_{\mathrm{F}} \rightarrow 3\varepsilon_{\mathrm{F}}$ and measured the friction variations. The resulting shear stresses ($0.09 \pm 0.02$ GPa and $0.08 \pm 0.03$ GPa) coincide with the shear stress obtained with unmodified parameters ($0.07 \pm 0.02$ GPa). This indicates that the influence of the $\varepsilon$ parameter on friction is negligible even for relatively large variations of $\varepsilon$ if the external pressure is large enough. There might be a smooth variation of the friction dependency on $\varepsilon$ for increasing pressure values that could be addressed in a future study.

# 10 Adhesive and Elastic Contributions to the CPES Profile for 0H/100F and 0H/100F with $\sigma_{\mathrm{F}} \rightarrow \sigma_{\mathrm{H}}$

The shear stress in the 0H/100F sliding system increases significantly if $\sigma_{\mathrm{F}}$ is replaced by $\sigma_{\mathrm{H}}$ (Fig. 4a of the main text). At the same time, an increase in the variation of the inter-slab distance $\Delta z$ is observed (Fig. 4b of the main text). In order to understand the relation between shear stress and $\Delta z$ (i.e. the geometric corrugation of the sliding interface), we elaborate how the CPES corrugation changes upon the $\sigma_F \rightarrow \sigma_H$ substitution. The CPES corrugation has two contributions that originate from: i) the variation of the elastic deformation along the sliding path and ii) the variation of adhesion along the sliding path. We note that, since the total height of the system stabilizes at a constant value during the dynamic simulations under normal load, the NEB simulations, which are used to determine the CPES corrugation along the sliding path, are performed with a fixed system height. As a result, a larger $\Delta z$

Table S2: Comparison of the elastic energy contribution $\Delta E_{elast}$ and the adhesive energy contribution $\Delta E_{adh}$ to the NEB energy barrier between $\Delta x \approx 2.9$ Å and $\Delta x \approx 3.5$ Å in Fig. 4b of the main text for 0H/100F and 0H/100F, where $\sigma_{\mathrm{F}}$ was replaced with $\sigma_{\mathrm{H}}$.

| | $\Delta E_{adh}$ (eV/Å$^2$) | $\Delta E_{elast}$ (eV/Å$^2$) | $\Delta E = \Delta E_{elast} + \Delta E_{adh}$ (eV/Å$^2$) |
|---|---|---|---|
| 0H/100F | 0.0004 | 0.0013 | 0.0017 |
| 0H/100F, $\sigma_{\mathrm{F}} \rightarrow \sigma_{\mathrm{H}}$ | 0.0030 | 0.0045 | 0.0075 |

along the sliding path can be expected to lead to a larger variation in mechanical energy due to the larger elastic deformations.

As an example, we consider the NEB energy barrier between $\Delta x \approx 2.9$ Å and $\Delta x \approx 3.5$ Å in Fig. 4b, which increases from 0.0017 eV/Å$^2$ to 0.0075 eV/Å$^2$ upon $\sigma_F \rightarrow \sigma_H$ substitution, and evaluate both the elastic and adhesive contributions. The difference between the energies required to separate the two slabs rigidly at the minimum and at the transition state corresponds to the adhesive part $\Delta E_{adh}$. The difference between the energies gained by relaxing the infinitely separated slabs in the minimum and in the transition state configurations are the elastic contribution $\Delta E_{elast}$ to the energy barrier. The results, listed in table S2, show that both contributions are significant. Upon $\sigma_F \rightarrow \sigma_H$ substitution, $\Delta E_{elast}$ increases by a factor of about 3.5, while $\Delta E_{adh}$ increases almost by almost one order of magnitude. This highlights that the large spatial extension of F terminations contribute to low friction in two ways, by reducing steric barriers that result in different elastic deformations during sliding and by keeping the surfaces apart to minimize adhesion energy variations.

# 11 Friction of "Less Commensurate" H/F-Terminated C(111) Tribosystems

The goal of this section is to understand how many H terminations of the 100H/0F system need to be replaced by F terminations in "less commensurate" C(111) systems (Fig. 6b of the main text) in order to achieve a frictional stress comparable to that of the 0H/100F system. To do so, we evaluate the frictional stress $\langle \tau \rangle$ of each mixed-terminated system using three different random arrangements of the terminations. As shown in Fig. S8, replacing about 40 % of the H terminations with F yields shear stress values that are comparable to the shear stress in the 100F/0H case.

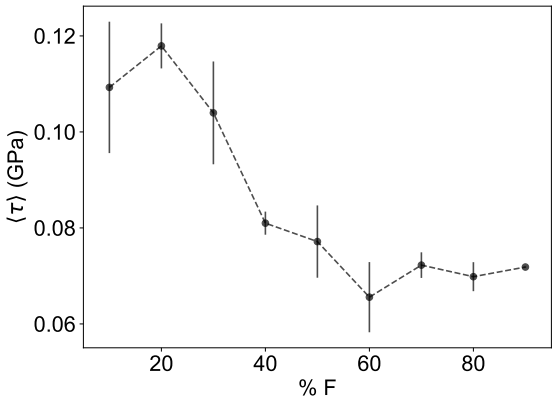


Figure S8: Shear stress $\langle\tau\rangle$ as a function of the fluorine termination content of H/F-terminated C(111) sliding interfaces. The arrangement of the terminations is randomized and the sliding direction has an angle of 19° with respect to the $[\overline{1}\overline{1}2]$ direction. Each data point corresponds to three simulations with different random arrangements of the terminations. Error bars correspond to the standard error of the mean of these three $\langle\tau\rangle$ values.

# 12 Tetrahedral Amorphous Carbon Systems

## 12.1 Bulk System

### 12.1.1 Melt-Quench Protocol

The tetrahedral amorphous carbon system was obtained by quenching liquid carbon from the melt. We used the screened REBO2 potential[17] which is well established for a-C systems.[18] The equations of motion were integrated using a time step of 0.1 fs. An initial random arrangement of about 53000 C atoms was equilibrated at 9000 K for 10 ps in a fixed volume corresponding to a density of 3.26 g/cm$^3$. The system was then quenched to 5000 K in 10 ps using a Langevin thermostat with a time constant of 0.5 ps and then quenched to 300 K in 15 ps using the same time constant. Next, an additional annealing step was performed by holding the system at 1000 K for 30 ps. Finally, we performed a geometry optimization to relax the system.

### 12.1.2 Force Field Parameters

To keep the number of force field parameters as small as possible, we define two types of bulk C atoms: (i) C atoms with coordination 4 are labelled as sp$^3$ C atoms; (ii) C atoms with coordination lower than 4 are labelled as sp$^2$ C atoms. We note that only 25 atoms in the system have a coordination lower than 3. As in the diamond case (see main text), bulk ta-C is described by harmonic bonds and angles. The bond lengths $r_{eq}$ for sp$^2$C$-$sp$^2$C bonds and sp$^3$C$-$sp$^3$C bonds are chosen to be 1.42 Å and 1.57 Å, respectively. This choice conserves the volume of the cell (i.e. the density) as obtained with the screened REBO2 potential. The equilibrium angle for angles centered on sp$^3$ C atoms is 109.5°, while the equilibrium angle for angles centered on sp$^2$ C atoms is 120.0°. Force constants are adjusted in order to

Table S3: Density, content of $sp^3$ C atoms and elastic properties of ta-C as determined experimentally and using the presented force field.

| | Experiment[19] | Force Field |
|---|---|---|
| Density (g/cm$^3$) | 3.26 | 3.26 |
| $sp^3$ (%) | 88 | 82 |
| Young's modulus (GPa) | 757 | 753 |
| Shear modulus (GPa) | 337 | 334 |
| Bulk modulus (GPa) | 334 | 337 |
| Poisson's ratio | 0.12 | 0.13 |

reproduce experimental values of the elastic constants, as shown in table S3. This yields the following parameters: $k_{r,\mathrm{sp3}} = 13.08$ eV/Å$^2$ for $sp^3$C−$sp^3$C bonds; $k_{r,\mathrm{sp2}} = 17.49$ eV/Å$^2$ for $sp^2$C−$sp^2$C bonds; $k_{\theta,\mathrm{sp3}} = 3.70$ eV/rad$^2$ for angles centered on $sp^3$ C atoms; $k_{\theta,\mathrm{sp2}} = 3.17$ eV/rad$^2$ for angles centered on $sp^2$ C atoms. The equilibrium bond length and force constant for $sp^2$C−$sp^3$C bonds are the arithmetic averages of the $sp^2$C−$sp^2$C and $sp^3$C−$sp^3$C values.

## 12.2 Surfaces

### 12.2.1 Chemical Termination of the Surfaces

Two different slabs are obtained from the bulk system by cutting at two different heights and removing the periodic boundary conditions in the direction perpendicular to the cutting plane. In order to obtain stable surfaces and allow recombination of dangling bonds that are created by creating the surfaces from the bulk systems, each system is kept at 300 K for 30 ps. Afterwards, each slab is relaxed and the remaining surface dangling bonds are terminated with hydrogen using the protocol below. For computational efficiency we use the REBO2 potential[20] without screening.

1. We create a list of all under-coordinated surface atoms. These are defined as atoms with a coordination smaller than four and a distance of at most 2 Å from the surface plane which is defined by the outermost atom.

2. A random under-coordinated atom is chosen from the list and a H atom is placed into its vicinity. Next, the whole system is relaxed using a maximal force threshold of 0.025 eV/Å. If the H adsorption is energetically favorable (compared to the chemical potential of H in $H_2$) the H atom is added to the system. If the new coordination of the C atom is four or the H adsorption is energetically unfavorable, the C atom is removed from the list. This procedure is iteratively executed until the list is empty.

F terminations are simply added by substituting H terminations. This ensures that the tribosystem compared in the main text have the same surface termination structure and coverage. The termination densities of the two ta-C slabs are 0.176 Å$^{-2}$ and 0.167 Å$^{-2}$, i.e. slightly smaller than in the C(111) case (0.183 Å$^{-2}$).

### 12.2.2 Force Field Parameters

We try to reuse the parameters for the C(111) terminations as much as possible. All $\sigma$ and $\varepsilon$ parameters of the H and F terminations, as well as their atomic charges, are the same as for H/F-terminated C(111). To ensure charge neutrality, H/F-terminated C atoms are assigned the countercharge of their terminations. C−H and C−F bonding parameters are the same as in the C(111) case. The equilibrium values of angles centered on $sp^2$C and $sp^3$C are 120° and 109.5°, respectively. $k_{\theta,\mathrm{HCH}}$ and $k_{\theta,\mathrm{CCH}}$ are identical to $k_{\theta,\mathrm{CCH}}$ for H/F-terminated C(111), $k_{\theta,\mathrm{FCF}}$ and $k_{\theta,\mathrm{CCF}}$ are identical to $k_{\theta,\mathrm{CCF}}$ for H/F-terminated C(111). $k_{\theta,\mathrm{HCF}}$ is defined as an arithmetic average of $k_{\theta,\mathrm{FCF}}$ and $k_{\theta,\mathrm{HCH}}$.

# 13 Quasistatic ta-C Sliding Simulations for the Determination of the CPES Corrugation

The (periodic) sliding interface of the ta-C systems has an area of 43.53 × 40.21 Å$^2$. As a result, an evaluation of the barriers along the sliding path using NEB calculations becomes unfeasible. For this reason, we perform quasi-static shear simulations to estimate the sum of the barriers along the sliding path. The ta-C surfaces are initially brought into contact and relaxed. To mimic the external load, the upper and lower rigid layers are fixed at the height that is measured during the dynamic simulations. Afterwards, the upper rigid layer is iteratively moved at least twice over the unit cell in the shear direction in steps of about 0.17 Å. After each step the whole system is relaxed and the potential energy of the system is measured. All barriers in the second sliding cycle (in order to get a perfectly periodic signal any initial "running-in" during the first cycle is omitted) are evaluated as indicated in Fig. S9. The sum of these barriers normalized by the cell length in the sliding direction is used as a measure of the corrugation and is the quantity that is plotted in Fig. 7c of the main text.

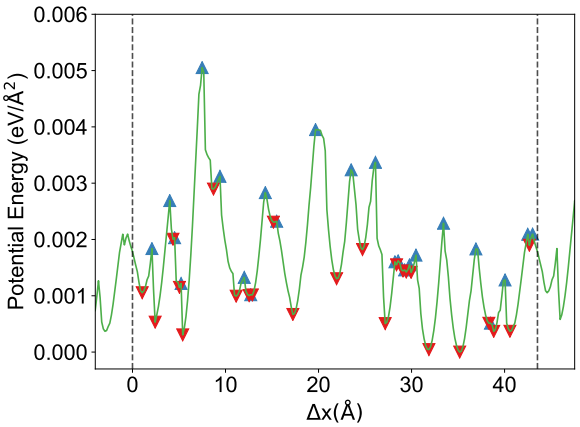


Figure S9: Example of normalized potential energy (green) during quasistatic sliding simulations for 0H/100F-terminated ta-C surfaces. Maxima (blue) and minima (red) are used in order to determine the sum of the barriers along the sliding path.

# 14 Friction of ta-C Systems

A detailed study of all possible parameters influencing friction of amorphous carbon surfaces is out of the scope of this study. The preliminary study summarized in Fig. 7b of the main text aims at understanding the relative relevance of steric and electrostatic interactions in analogy to the study performed on C(111) surfaces. In order to improve the statistical relevance of this preliminary study, we performed the simulations described in Fig. 7b, this time using a sliding direction perpendicular to the original one. The result is shown in Fig. S10. While friction values clearly depend on the particular sliding direction, the main trends shown in Fig. 7b are confirmed: (i) Steric effects (green, red and orange bars) dominate over electrostatic effects (blue bars); (ii) maximum shear stress values are obtained for mixed terminations.

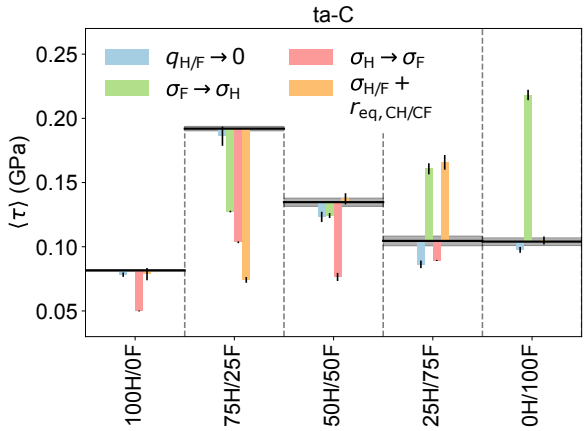


Figure S10: Averaged shear stresses $\langle\tau\rangle$ for ta-C sliding systems with different H/F terminations (black lines). The grey-shaded areas show error bars for these values. Blue bars show the $\langle\tau\rangle$ variation when the MD sliding simulations is performed after setting the atomic charge values to zero. Red and green vertical bars show the $\langle\tau\rangle$ variations due to the $\sigma_H \rightarrow \sigma_F$ and $\sigma_F \rightarrow \sigma_H$ substitutions, respectively. Orange bars correspond to the shear stress variation due to a combined $\sigma_H \leftrightarrow \sigma_F$ and $r_{\mathrm{eq,CH}} \leftrightarrow r_{\mathrm{eq,CF}}$ exchange. The systems are identical to the ones used in Fig. 7b, but the sliding direction is rotated by 90°.

# 15 Elastic Deformation of Surface Terminations: A Comparison between Randomly Terminated Diamond and ta-C

There are two major differences in the roughness of H/F-terminated diamond and ta-C surfaces:

(i) In perfectly flat, non-defective C(111) surface, surface carbon atoms ($C_{\mathrm{surf}}$) have the same $z$ coordinate and therefore there are only two possible heights for the terminations: $z(\mathrm{H}) = z(C_{\mathrm{surf}}) + d_{\mathrm{CH}}$ and $z(\mathrm{F}) = z(C_{\mathrm{surf}}) + d_{\mathrm{CF}}$. Due to taC's amorphous

structure, its surface has an intrinsic roughness. Therefore the $z$ coordinate of the termination can vary continuously between the peak and the valley.

(ii) On C(111) surfaces the arrangement of the terminations is a perfect lattice with C-H and C-F bonds oriented perpendicular to the surface plane. For ta-C both the arrangement and the orientation of the C-H/C-F bonds are disordered.

The peak-to-valley distance on ta-C, measured as the difference between the by maximum and the minimum position of the terminations in the direction perpendicular to the surface plane ranges between 2.6 and 3.9 Å (for ta-C samples and H/F combinations considered in the manuscript). In diamond the pick-to-valley distance is zero for 100H/0F and 0H/100F surfaces, while it is simply given by the bond- length difference between C-H and C-F (0.3 Å) for mixed terminations.

In a publication about tight-binding simulations of friction in F/H-terminated DLC films, Bai et al. [21] observed that partial substitution of H with F on DLC surfaces causes an increase in friction (compatible with our observations). They ascribe this increase in friction to the fact that the larger F atoms constitute "larger atomic-scale asperities" leading to larger deformations due to steric collisions between terminations during sliding. We note that this increase would not occur in diamond due to the perfectly flat surfaces with only two possible termination heights. Due to the very low elastic compliance of diamond contacts, a few F atoms are sufficient to keep the two diamond surfaces apart and to avoid these increased collisions.

To verify whether this explanation is reasonable, we performed further analysis and some new simulations to quantify the magnitude of collisions between terminations and their relation to friction in both diamond and ta-C.

For our line of argument, two important aspects described in the manuscript are relevant:

(i) The shear stress $\langle\tau\rangle_{\mathrm{MD}}$ correlates linearly with the CPES corrugation measured as the normalized sum of energy barriers along the sliding path ($\langle\tau\rangle_{\mathrm{ideal}}$) for both diamond (Fig. 3c) and ta-C (Fig. 7c).

(ii) The corrugation of the CPES is caused by elastic deformations which are necessary to avoid steric "collisions" between terminations of opposite surfaces (Fig. 5). The elastic deformation is completely determined by LJ repulsion interactions and is caused by the displacements of the terminations atoms in order to avoid "heads-on" collisions with the terminations of the opposite surface.

Next, we measure the magnitude of the terminations displacements along the sliding path and check whether it correlates with the CPES corrugation $\langle\tau\rangle_{\mathrm{ideal}}$ (and therefore with the shear stress $\langle\tau\rangle_{\mathrm{MD}}$). Since NEB simulations to determine $\langle\tau\rangle_{\mathrm{ideal}}$ are unfeasible for ta-C, due to the large size of the simulation cell and the large number of barriers along the sliding path, we use the energetic corrugation of the ta-C surfaces as obtained by quasistatic shear simulations (see section 13). For the randomly terminated diamond case, we omit the 19° angle with respect to the $x$-axis shear along the $x$-axis instead to reduce the length of periodicity to the length of the supercell (43.53 Å). Note that even though the obtained shear stresses in dynamic simulations (100H/0F: $0.21 \pm 0.01$ GPa, 50H/50F: $0.11 \pm 0.02$ GPa, 0H/100F: $0.07 \pm 0.02$ GPa) are slightly larger compared to the incommensurate 19° angle

case (100H/0F: $0.13 \pm 0.04$ GPa, 50H/50F: $0.09 \pm 0.02$ GPa, 0H/100F: $0.06 \pm 0.01$ GPa), there is no shear stress peak for the mixed terminated H/F-terminated case, which is the main difference between incommensurate sliding in diamond and ta-C.

Fig. S11 shows $\langle\tau\rangle_{\text{ideal}}$ plotted as a function of the average termination displacements on the $xy$ plane for both C(111) and ta-C. The displacement of the terminations during sliding is a direct measure of the steric hindrances occurring during sliding. For this purpose, we calculate the length of the displacement vector in the surface plane for every termination with respect to far separated, relaxed slabs and average over the quasistatic trajectory within one cell length and over all terminations. There is a good linear correlation between both quantities for both diamond and ta-C.

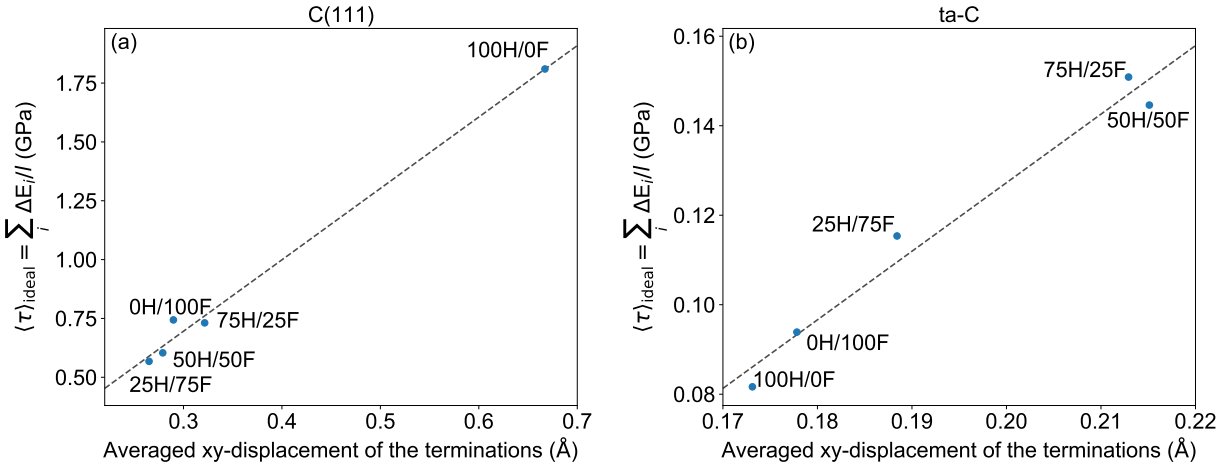


Figure S11: $\langle\tau\rangle_{\text{ideal}}$ as a function of the averaged displacement of the terminations in the surface plane for (a) randomly H/F-terminated C(111) surfaces sheared along the $[\overline{1}12]$ direction and (b) ta-C.

This confirms that higher friction is due to larger magnitudes of the terminations displacements (i.e. more pronounced collisions). A comparison between diamond and ta-C suggests that the steric hindrance that determines friction in the investigated system is differently affected by a H→F substitution. For H/F-terminated diamond surfaces, around 40% percent F is usually enough to keep the surfaces apart. Due to the discrete set of termination planes and the perfectly flat surface, interdigitation of the surfaces becomes very unlikely, even if the sliding direction is commensurate with respect to the H/F rows. In contrast, for ta-C the average displacement of the terminations increases for mixed-terminated cases. Even though the partial substitution of H with F contributes to push the surfaces further apart (the height of the systems in the dynamic simulations increases with increasing F content), isolated fluorine atoms can act as obstacles for terminations of the counter-surface such that the steric hindrance and the shear stress increase (in line with the hypothesis of Bai et al. [21] mentioned above).

Note that $\langle\tau\rangle_{\text{ideal}}$ and the displacement values in Fig. S11 are larger in the diamond than in ta-C. Despite the randomly arranged H/F surface terminations in the mixed cases,

the sliding in the diamond system occurs along the $x$ direction and therefore the system is commensurate in the 100H/0F and in the 0H/100F cases. Also in the mixed cases the two diamond lattices slide in a commensurate way. That is the reason why we used a rotation of the sliding direction of 19° with respect to the $x$ direction in the main text. Moreover, the stiffness of the diamond and the DLC systems is different. This makes the comparison of the absolute friction values between the two systems impossible.

A future study could address the different contributions due to atomic-scale roughness, and to the disordered distribution and orientation of the terminations. This could be done step-by-step, by separately considering diamond surfaces with different orientation of the surface terminations (e.g. C(100)) and then diamond surfaces with various degrees of surface defects that alter their ordered surface structure.

# 16 Calculation of the CPES with Different Corrections for the Dispersion Interactions

In order to assess the robustness of the CPES obtained by means of the PBE-TS09 method,[15] we recalculated the CPES along a straight sliding path (Fig. 1e in the main text) using the PBE-D3 method of Grimme[22] and the PBE-TS09-SCS approach with self-consistent screening by Tkatchenko et al.[23] as implemented in VASP.[24] VASP uses a plane wave basis set to expand the valence electron Kohn-Sham wavefunctions. A cut-off energy of 520 eV was used for the plane wave expansion in all simulations. The effect of core electrons was described within the projector-augmented wave method (PAW).[25,26] In order to take into account the periodicity of the investigated systems, the Ewald summation was applied to the D3 and TS09-SCS dispersion correction terms.[27]

The results are illustrated in Fig. S12 and the normalized sum of the energetic barriers as measure of the ordering of the CPES corrugation is given in table S4. Despite the differences in the absolute energy values, the ordering of the barrier heights and of the CPES corrugation values on which the manuscript's conclusions are based do not depend on the choice of the van der Waals correction.

Table S4: $\langle\tau\rangle_{\text{ideal}} = \sum_i \Delta\text{E}_i/l$ as a function of the applied dispersion correction, where $\Delta\text{E}_i$ are the CPES barriers shown in Fig. S12, and $l$ is the length of the unit cell in sliding direction.

| | PBE-TS09 | PBE-D3 | PBE-TS09-SCS |
|---|---|---|---|
| 0H/100F (GPa) | 0.09 | 0.04 | 0.04 |
| 25H/75F (GPa) | 0.12 | 0.07 | 0.08 |
| 50H/50F-A (GPa) | 0.15 | 0.08 | 0.09 |
| 100H/0F (GPa) | 0.16 | 0.08 | 0.12 |
| 75H/25F (GPa) | 0.37 | 0.21 | 0.24 |
| 50H/50F-B (GPa) | 0.47 | 0.31 | 0.36 |

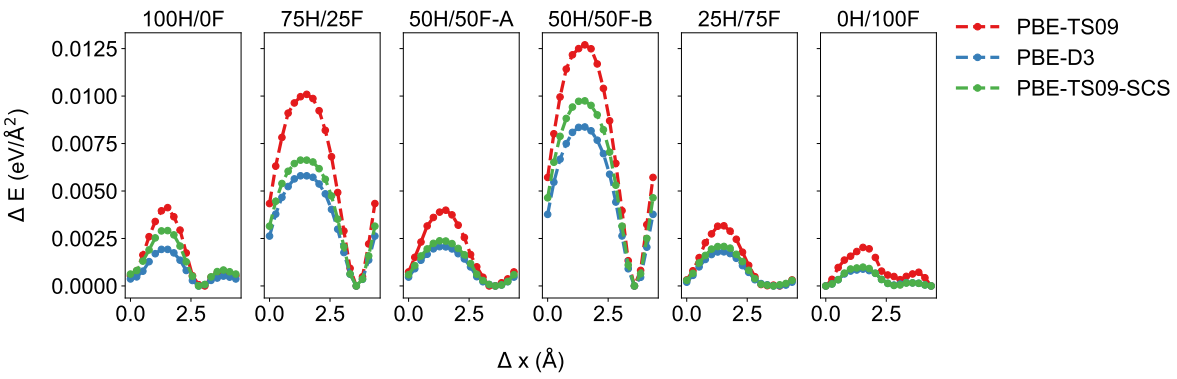


Figure S12: Corrugation of the CPES along a straight sliding path (see Fig. 1e in the main text) as calculated with the PBE-TS09,[15] the PBE-D3[22] and the PBE-TS09-SCS[23] methods.

# References


[1] Elstner, M.; Porezag, D.; Jungnickel, G.; Elsner, J.; Haugk, M.; Frauenheim, T.; Suhai, S.; Seifert, G. *Physical Review B* **1998**, *58*, 7260–7268.

[2] `https://github.com/Atomistica/atomistica`.

[3] Kuwahara, T.; Moras, G.; Moseler, M. *Physical Review Letters* **2017**, *119*, 096101.

[4] Konicek, A. R.; Grierson, D. S.; Gilbert, P. U. P. A.; Sawyer, W. G.; Sumant, A. V.; Carpick, R. W. *Physical Review Letters* **2008**, *100*, 235502.

[5] Pastewka, L.; Moser, S.; Moseler, M. *Tribology Letters* **2010**, *39*, 49–61.

[6] O'Hagan, D. *Chemical Society Reviews* **2008**, *37*, 308–319.

[7] Jorgensen, W. L.; Maxwell, D. S.; Tirado-Rives, J. *Journal of the American Chemical Society* **1996**, *118*, 11225–11236.

[8] Zouboulis, E. S.; Grimsditch, M.; Ramdas, A. K.; Rodriguez, S. *Physical Review B* **1998**, *57*, 2889–2896.

[9] Watkins, E. K.; Jorgensen, W. L. *The Journal of Physical Chemistry A* **2001**, *105*, 4118–4125.

[10] Mayrhofer, L.; Moras, G.; Mulakaluri, N.; Rajagopalan, S.; Stevens, P. A.; Moseler, M. *Journal of the American Chemical Society* **2016**, *138*, 4018–4028.

[11] Li, Q.; Liu, X.-Z.; Kim, S.-P.; Shenoy, V. B.; Sheehan, P. E.; Robinson, J. T.; Carpick, R. W. *Nano Letters* **2014**, *14*, 5212–5217.

[12] Bouchet, M.-I. D. B.; Zilibotti, G.; Matta, C.; Righi, M. C.; Vandenbulcke, L.; Vacher, B.; Martin, J.-M. *The Journal of Physical Chemistry C* **2012**, *116*, 6966–6972.

[13] Zhong, W.; Tománek, D. *Physical Review Letters* **1990**, *64*, 3054–3057.

[14] Wolloch, M.; Levita, G.; Restuccia, P.; Righi, M. *Physical Review Letters* **2018**, *121*.

[15] Tkatchenko, A.; Scheffler, M. *Physical Review Letters* **2009**, *102*.

[16] Krylov, S. Y.; Frenken, J. W. M. *Physica Status Solidi (b)* **2014**, *251*, 711–736.

[17] Pastewka, L.; Pou, P.; Pérez, R.; Gumbsch, P.; Moseler, M. *Physical Review B* **2008**, *78*, 161402.

[18] Pastewka, L.; Mrovec, M.; Moseler, M.; Gumbsch, P. *MRS Bulletin* **2012**, *37*, 493–503.

[19] Ferrari, A. C.; Robertson, J.; Beghi, M. G.; Bottani, C. E.; Ferulano, R.; Pastorelli, R. *Applied Physics Letters* **1999**, *75*, 1893–1895.

[20] Brenner, D. W.; Shenderova, O. A.; Harrison, J. A.; Stuart, S. J.; Ni, B.; Sinnott, S. B. *Journal of Physics: Condensed Matter* **2002**, *14*, 783–802.

[21] Bai, S.; Murabayashi, H.; Kobayashi, Y.; Higuchi, Y.; Ozawa, N.; Adachi, K.; Martin, J. M.; Kubo, M. *RSC Advances* **2014**, *4*, 33739.

[22] Grimme, S.; Antony, J.; Ehrlich, S.; Krieg, H. *The Journal of Chemical Physics* **2010**, *132*, 154104.

[23] Tkatchenko, A.; DiStasio, R. A.; Car, R.; Scheffler, M. *Physical Review Letters* **2012**, *108*.

[24] Kresse, G.; Furthmüller, J. *Physical Review B* **1996**, *54*, 11169–11186.

[25] Kresse, G.; Joubert, D. *Physical Review B* **1999**, *59*, 1758–1775.

[26] Blöchl, P. E. *Physical Review B* **1994**, *50*, 17953–17979.

[27] Kerber, T.; Sierka, M.; Sauer, J. *Journal of Computational Chemistry* **2008**, *29*, 2088–2097.